Available online at www.sciencedirect.com
ScienceDirect
Continental Shelf Research 28 (2008) 710–725
CONTINENTAL SHELF RESEARCH
www.elsevier.com/locate/csr

Suspended sediment fluxes at an intertidal flat: The shifting influence of wave, wind, tidal, and freshwater forcing

Stefan A. Talke[a,*], Mark T. Stacey[b]

[a]Institute for Marine and Atmospheric research, University of Utrecht, Princetonplein 5, 3584 CC Utrecht, The Netherlands
[b]Department of Civil and Environmental Engineering, University of California at Berkeley, Berkeley, CA 94720, USA

Received 2 January 2007; received in revised form 27 October 2007; accepted 7 December 2007
Available online 23 December 2007

Abstract

Using in situ, continuous, high frequency (8–16 Hz) measurements of velocity, suspended sediment concentration (SSC), and salinity, we investigate the factors affecting near-bed sediment flux during and after a meteorological event (cold front) on an intertidal flat in central San Francisco Bay. Hydrodynamic forcing occurs over many frequency bands including wind wave, ocean swell, seiching (500–1000 s), tidal, and infra-tidal frequencies, and varies greatly over the time scale of hours and days. Sediment fluxes occur primarily due to variations in flow and SSC at three different scales: residual (tidally averaged), tidal, and seiching. During the meteorological event, sediment fluxes are dominated by increases in tidally averaged SSC and flow. Runoff and wind-induced circulation contribute to an order of magnitude increase in tidally averaged offshore flow, while waves and seiching motions from wind forcing cause an order of magnitude increase in tidally averaged SSC. Sediment fluxes during calm periods are dominated by asymmetries in SSC over a tidal cycle. Freshwater forcing produces sharp salinity fronts which trap sediment and sweep by the sensors over short (~30 min) time scales, and occur primarily during the flood. The resulting flood dominance in SSC is magnified or reversed by variations in wind forcing between the flood and ebb. Long-term records show that more than half of wind events (sustained speeds of greater than 5 m/s) occur for 3 h or less, suggesting that asymmetric wind forcing over a tidal cycle commonly occurs. Seiching associated with wind and its variation produces onshore sediment transport. Overall, the changing hydrodynamic and meteorological forcing influence sediment flux at both short (minutes) and long (days) time scales.

Keywords: Intertidal mudflat; Sediment transport; Waves; Tides; Seiching; USA; California; San Francisco Bay

1. Introduction

Intertidal flats form a boundary between land and sea, and are important feeding grounds for birds, fish, and other biota. Moreover, due to their proximity to cities and industrial areas, intertidal flats may contain buried contaminants that are uncovered by storm events and long-term morphological change. Thus, the physical processes that create, erode, and rework intertidal flats are immensely important from both an ecological and practical viewpoint.

Previous studies have suggested that the primary forces shaping intertidal flats are wind-induced waves and tidal currents. The shifting influence of wind has generally been reduced to three distinct levels of forcing conditions: stormy, windy, and calm (Shi and Chen, 1996; Le Hir et al., 2000; Janssen-Stelder, 2000). During storms, large waves are observed to erode sediment and keep sediment in suspension during the slack tide, which is then available to be transported offshore during the ebb (Le Hir et al., 2000; Dyer et al., 2000; Bassoullet et al., 2000; Andersen and Pejrup, 2001). Storms may also deposit sediments onto upland marshes (e.g., Yang et al., 2003, and list therein). During windy periods, local erosion generally results in offshore transport (Christie et al., 1999; Dyer et al., 2000; de Jonge and van Beusekom, 1995), though net transport can be onshore as well (e.g., de Haas and Eisma, 1993).

*Corresponding author. Present address: Civil & Environmental Engineering, University of Washington, 201 More Hall, Box 352700 Seattle, WA 98195-2700, USA.
E-mail addresses: stalke@u.washington.edu (S.A. Talke), m.stacey@berkeley.edu (M.T. Stacey).

0278-4343/$ - see front matter © 2008 Elsevier Ltd. All rights reserved.
doi:10.1016/j.csr.2007.12.003

During calm periods, net transport is observed to be onshore (Black, 1998; Christie et al., 1999; Dyer et al., 2000; Le Hir et al., 2000; Ridderinkhof et al., 2000), which is attributed to settling lag and scour lag effects (Christie et al., 1999). Sediment is observed to be eroded during the flood tide, is transported shoreward, and settles out during the high-water slack period (Christie et al., 1999; de Haas and Eisma, 1993; Ridderinkhof et al., 2000). Because ebb currents are insufficient to resuspend and transport all the recently deposited sediment (even in an ebb dominated estuary such as the Dollard, NL), accretion occurs in calm periods (Dyer et al., 2000).

Models of sediment transport have provided important insights into intertidal processes by focusing on the effects of tidal currents (Friedrichs and Aubrey, 1996; Pritchard and Hogg, 2003; Pritchard et al., 2002), or the combined affect of winds and tidal currents (Ridderinkhof, 1998; Roberts et al., 2000; Waeles et al., 2004). Sediment fluxes are found to occur due to tidal asymmetries in velocity (e.g., Ridderinkhof, 1998; Roberts et al., 2000; Pritchard et al., 2002) and due to settling lag effects (e.g., Pritchard and Hogg, 2003). Ridderinkhof (1998) concludes that asymmetries in tidal velocities (rather than waves) set the direction of sediment flux, and that waves reduce net sediment flux by keeping sediment in suspension over a tidal cycle. Waeles et al. (2004) finds that even small (but constantly applied) waves of 5 cm cause an export of sediment that is balanced by input at the seaward boundary. All models that include wave effects apply constant forcing over a tidal period (e.g., Ridderinkhof, 1998; Roberts et al., 2000; Waeles et al., 2004).

Other factors besides wind waves and tidal currents are observed to play a role in sediment erosion and transport over a tidal time scale. Ridderinkhof et al. (2000) and de Haas and Eisma (1993) note that storm surge increases suspended sediment concentration (SSC) and offshore transport in the Ems/Dollard estuary. Storm surge also increases the influx of sediments to upland marshes, particularly during spring tides (Yang et al., 2003). Christiansen et al. (2006) found that asymmetries in tidal velocity caused by winds of 4–12 m/s dominated sediment fluxes at a tidal flat in the Wadden Sea. Freshwater flow from upland watersheds or local rain runoff affects the mean current, as can local circulation patterns, nonlinear waves (Stokes drift), wind stress, and many other sources (Le Hir et al., 2000). Changes to the supply of sediment (Ridderinkhof et al., 2000; Wright and Schoellhamer, 2004) or the critical stress of erosion (Kornman and de Deckere, 1998; Staats et al., 2001; O'Brien et al., 2000; Dyer, 1998) are important components of the long-term sediment balance. All these factors show that erosion, deposition, and transport are subject to many changeable parameters.

In this contribution, we explore the subtle effects of changes in hydrodynamic and meteorological forcing from short time scales (wave time scale) to longer time scales (days) on an intertidal flat in San Francisco Bay. We investigate the mechanisms that elevate SSC, including waves, tidal currents, seiching motions, and freshwater forcing, and evaluate the time scales over which SSC and velocity vary. In turn we highlight how variations at both tidally averaged and intra-tidal time scales affect net sediment fluxes during a meteorological event (cold front) and a relatively calmer period. We show that the relative phasing (timing) and time scales of wind, tidal, and freshwater forcing can completely alter the net flux of sediment in the intertidal zone, even between consecutive tidal periods.

In Section 2 we describe the experiment site and measurement methods, while in Section 3 we describe the hydrographic results and explore the variations of SSC and sediment flux. In Section 4 we analyze sediment flux at the tidally averaged and tidally varying time scales, and the conclusions are presented in Section 5.

2. Methods

The intertidal flat we investigate in this study is situated in the central San Francisco Bay near the city of Richmond, CA (Fig. 1a). Along its east and west borders, the intertidal flat is fringed by marshland (Fig. 1b) that lies behind an outer seawall. The northern border is a rip-rap seawall. Two subtidal channels drain the upland marsh system and combine together within the intertidal flat. The southern side of the intertidal flat, roughly 200 m in diameter, is open to the central San Francisco Bay. The sediment is dominated by fine sand and silt, and the shape of the mudflat morphology is convex upwards, consistent with an accretionary flat (Dyer, 1998; Le Hir et al., 2000; Kirby, 2000). Ripples with a wavelength of 0.05–0.06 m and a height of 0.01–0.02 m occur on the flat.

Over a 4-day period beginning at 16:00 h (local time) on April 11, 2003 and ending at 17:00 h on April 15, 2003 we deployed an array of hydrodynamic sensors on a sawhorse frame (Fig. 2) located at the opening of the flat to the bay (see Fig. 1). The frame was located about 50 m west of the subtidal channel, and oriented along the primary (North–South) stream axis. The frame is thus optimally oriented to observe fluxes between the central bay and the flat. On the frame we deployed six acoustic doppler velocimeters (ADVs), three optical backscatter sensors (OBS) from D&A instruments, three conductivity–temperature–depth sensors (CTDs), and two combined OBS/fluorometers. The OBS was calibrated by Ralston (2005) using estimates of SSC found from co-located, in situ water samples.

The velocimeters and turbidity sensors were located at heights between 0.01 and 0.35 m off the bed, and measured a new, synchronous 'burst' of data every 10 min. Nearly continuous velocity data (burst length of 590 s) was measured at heights of 0.16 and 0.28 m at a frequency of 8 Hz, and was synchronized with OBS sensors at 0.05 and 0.19 m. The accuracy of the velocimeters is estimated by the manufacturers to be 0.001 m/s. Because of memory and battery constraints, the remaining velocimeters measured for burst lengths of either 188 s (side-mounted) or 345 s.

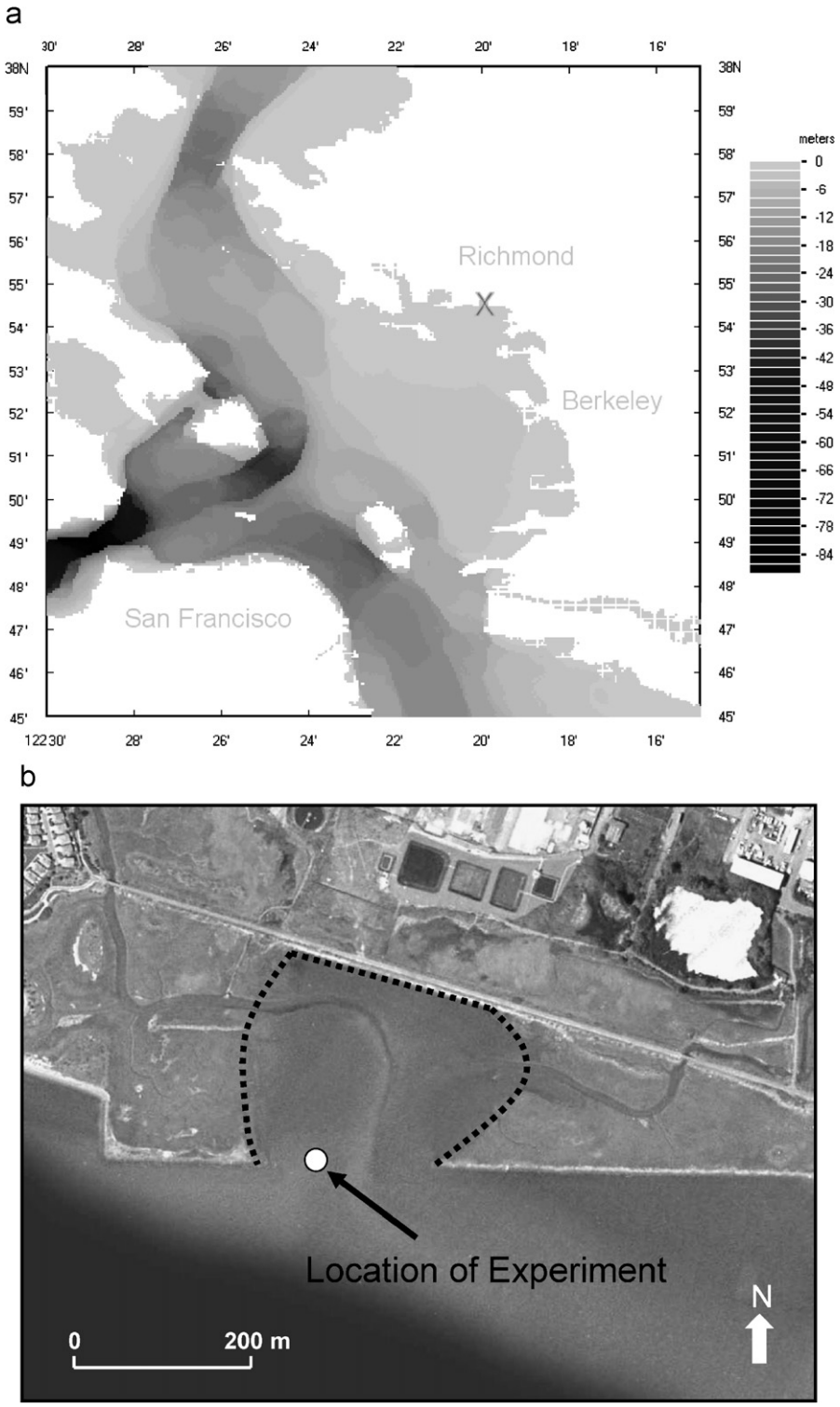

Fig. 1. (a) Location map of experiment in terms of latitude and longitude. The location of the experiment is marked with an 'X'. (b) Location of the instrument frame on the intertidal mudflat near the Richmond Field Station. The approximate borders of the mudflat with the intertidal marsh and the multi-use trail on the north side are denoted by the dotted line.

A small portion (order of 10–20 min) of each flood and ebb period was missed until the sensors were immersed. Additionally, the side-mounted velocimeters (0.1 and 0.33 m off bed), the two lower downward facing velocimeters (0.01 and 0.05 m off bed), and the lower OBS (0.05 m off bed) failed during the large cold front that occurred from April 11–13, 2003. Finally, during the cold front, changes to the relative bed-level of 0.05 to 0.1 m (the frame settled into the sediment) biased velocity and SSC measurements. The frame was repositioned relative to the

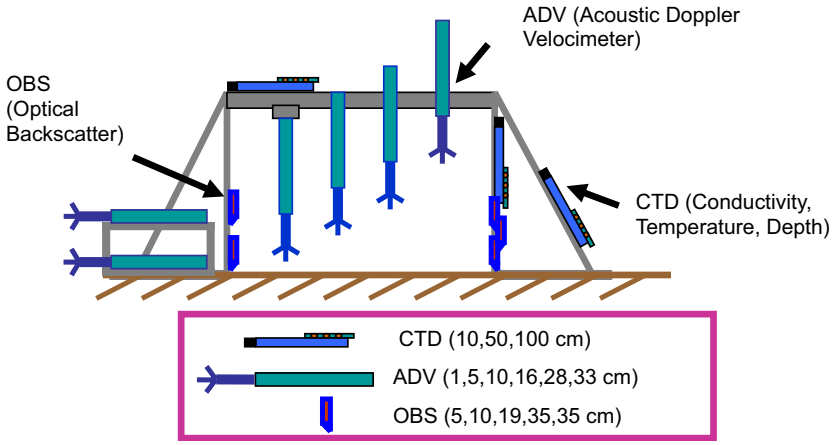

Fig. 2. Depiction of experimental set-up. Four downwards facing velocimeters were focussed 1, 5, 16, and 28 cm from the bed, while two sideways pointed velocimeters were focused at 10 and 33 cm off the bed. Five optical backscatter and three CTD instruments were placed as depicted in the figure.

bed after tide 4 to the initial specifications. Because of the data limitations, we focus on mechanisms of near-bed suspended sediment transport for the velocity/SSC pair deployed at 0.16 and 0.19 m, realizing that the height off the bed was O(0.1 m) during portions of the meteorological event.

We obtained hourly wind speed data from a meteorological station located ~1 km from the experiment site (Bay Area Air Quality Management District station 2950). Water level data were obtained from NOAA buoy 9414863 at the Chevron Oil Pier in Richmond. The publicly available tidal prediction software Jtides was used to compare predicted tidal levels to the actually measured tidal levels.

3. Results

Below we describe the hydrodynamic conditions prevalent during the experiment, and the sediment fluxes resulting from them. Because hydrodynamic conditions varied during the meteorological event (hours 0–50) and afterwards (hours 50–100), we summarize the hydrographic conditions in Figs. 3 and 4, respectively.

3.1. Hydrographic conditions

The central San Francisco Bay is forced by semi-diurnally varying tides with a maximum tidal range of ~2 m. During the first four tidal periods (Fig. 3a) of the experiment, the diurnal inequality is evident in the water-level amplitude (1.1–1.5 m), while by contrast the second four tides are nearly equal in amplitude (~1.5 m; Fig. 4a). The cross-shore, North–South tidal current V_{30}, as measured by a 30 min moving average, typically exhibits a maximum of 0.07–0.11 m/s with-in an hour of wetting or drying (see Figs. 3b and 4b), with the exception of an ebb flow of 0.25 m/s during the late ebb at $t = 20$–21 h (Fig. 3b).

Between April 11 and 13, 2003, a large cold front passed through the San Francisco Bay area. The peak of the meteorological event occurred between $t = 11$ and 19 h from the start of the experiment (i.e., during tide 2), with sustained winds of greater than 9 m/s (see Fig. 3c). Wind velocity reduced to a range of 4.5–7 m/s between hour 20 and hour 35, and to 4–6 m/s between hour 40 and hour 50. After the meteorological event, periods of moderate wind (3–5 m/s) occur between hours 50–52, hours 70–80, and hours 90–100. Between $t = 53$ and 88 h, wind was directed offshore (from North to South), as indicated by the dotted line.

A comparison of measured and predicted water levels show that winds caused a surge of ~0.25 m by $t = 20$ h, and reached a maximum of ~0.3 m at $t = 30$ h. Elevated water levels persisted through tide 4 (0.2 m at High Water (HW)) and tide 5 (0.06 m at HW) but became insignificant for tides 6–8. The surge coincided with seiching motions with velocities of 0–0.15 m/s and a period of ~500–1000 s. These seiching motions occur primarily during tides 2–5, and are shown by the envelope created by the 1-min mean velocity (Fig. 3b and 4b). As wind set-up disappears during tides 6–8, seiching motions become small.

Precipitation from the meteorological event increased the freshwater discharge in the subtidal creek, and began lowering salinity concentrations starting at $\sim t = 17$ h. During the meteorological event, large variation between bay water (>20 psu) and fresher water (<10 psu) were observed during wetting and drying. The effect of freshwater discharge was also observed at HW, as salinity decreased from 25.8 psu during tide 1 to a minimum of 23.2 psu during tide 3 (Fig. 3d). After the meteorological event, the salinity at HW slowly increases, from 24.3 psu at $t = 55$ h to 26.1 psu at $t = 92$ h (Fig. 4d). Similarly, the differences in salinity over a tidal period lessen.

As shown in Fig. 3e and 4e, the characteristic profile of SSC over an immersed period includes a period of elevated sediment concentration during the flood, a reduction during the slack period, and a corresponding increase during the ebb (see Fig. 4e). Overall, the tidally averaged concentration increases from 0.11 kg/m^3 during tide 1 to a

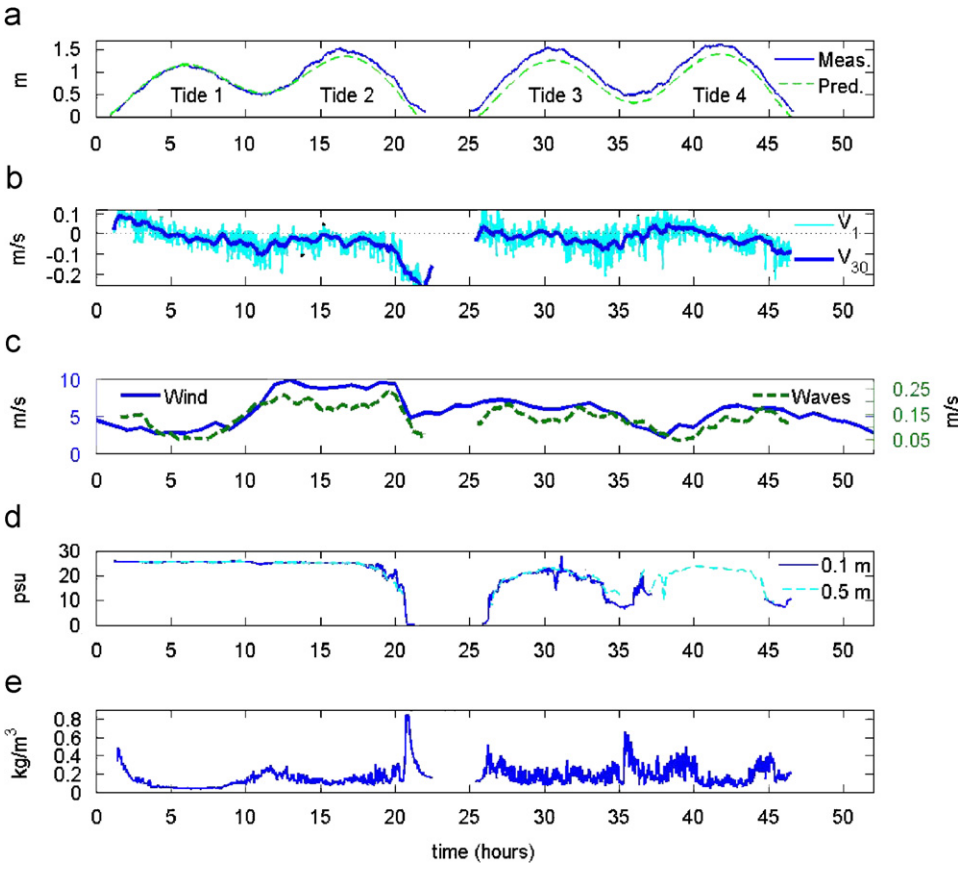

Fig. 3. Plots of (a) predicted and measured tides, (b) mean velocity, (c) wind and root-mean-square (rms) wave velocity, (d) salinity, and (e) suspended sediment concentration during a meteorological event (cold front). Zero hours refers to the start of the experiment at 16:00 h on April 11, 2003. In (b), both a 1 min block average (V_1) and a 30 min moving average (V_{30}) are displayed, and zero velocity is marked with a dotted line. The rms wave velocity is calculated after removing the 1 min mean velocity over blocks of 20 min.

peak of 0.19 kg/m^3 during tide 4, then reduces to 0.02 kg/m^3 by tide 7 (post-event). The source of variation in SSC over the experiment is the focus of the next section.

The evolution of wave orbital velocity and energy over the experiment is depicted in Figs. 3c, 4c and 5. The rms wave orbital velocity (estimated using an averaging time of 20 min after removing the 1 min mean velocity), decreases from a maximum of 0.24 m/s during the meteorological event to a maximum of 0.12 m/s in tides 5–8 (compare Figs. 3c and 4c). Near-bed wave energy was typically smallest at high tide since orbital motions decay more with depth during periods of HW (for the same wave conditions).

Fig. 5 compares the power spectrum of velocity during the flood and ebb period of each tidal period. Three bands of energy are evident: locally forced wind waves between 0.25 and 1 Hz, offshore ocean swell between 0.05 and 0.15 Hz, and intra-tidal motions between 3×10^{-3} and 8×10^{-4} Hz. Wind-induced wave energy is largest during tide 2, and decreases in spectral energy and average period ($T = 1/f$) occur as wind forcing decreases in succeeding tides (see also Fig. 3c). After the flood of tide 5, no appreciable wind-wave energy is evident until the ebb of tide 8. However, waves at the ocean swell frequency persist after local wind forcing vanishes (see also Talke and Stacey, 2003), and are the largest component of wave forcing from the ebb of tide 5 through the flood of tide 7. At lower frequencies, two peaks of energy are persistently found at periods of 500 s (2×10^{-3} Hz) and at 900–1000 s. These intra-tidal motions, which we collectively call 'seiching', are largest during the windy periods from tide 1 through tide 5. Differences in energy between flood and ebb are characteristic for all energy bands, and are particularly well defined for tides 4, 5, and 8 (wind waves), tides 5 and 7 (ocean swell) and tides 4, 7 and 8 (infra-tidal motions).

3.2. Analysis of SSC on flat

In this section we investigate whether wind causes the variation in waves and SSC at the experiment site by developing a regression between wind, wind waves, and SSC (Fig. 6). Fig. 6c shows the least-squares fit to a scatter plot of the 1 h mean wind energy and the 1 h mean wind-wave energy. Because the fit of the line is good ($R^2 = 0.78$), our measurements indicate that on average, wave energy is linearly related to wind forcing. However, the scatter in the data indicates that other factors (such as spatial and temporal variation in the instantaneous wind field, changes

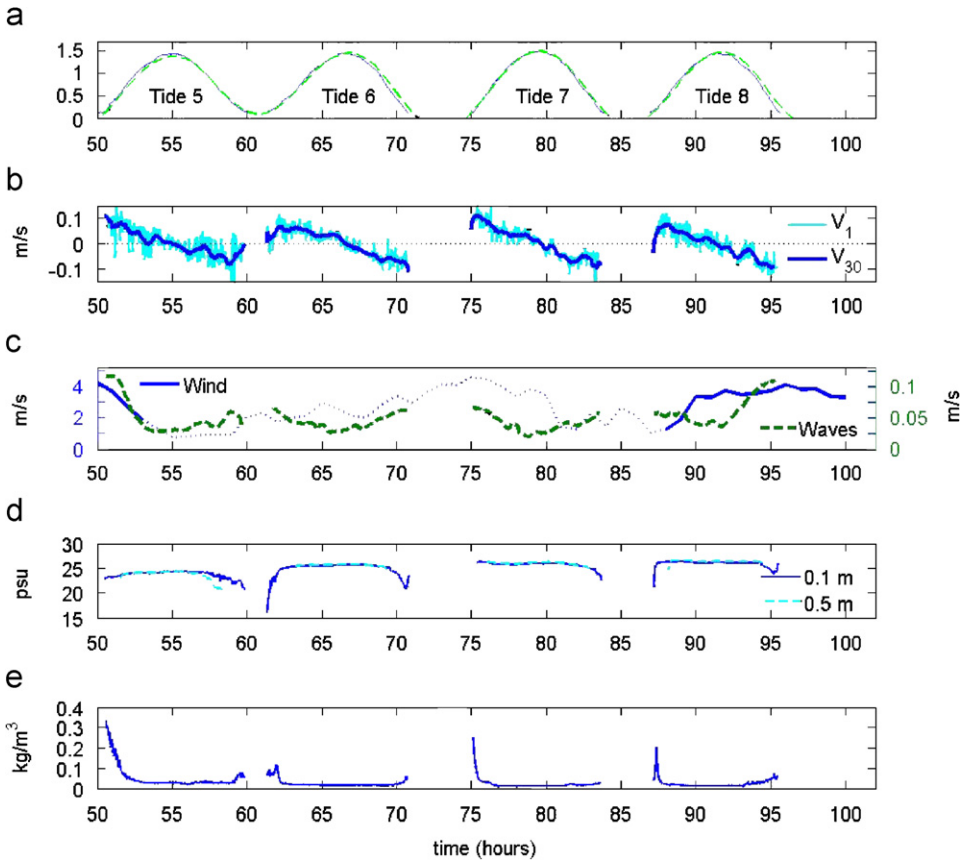

Fig. 4. Plots of (a) predicted and measured tides, (b) mean velocity, (c) wind and root-mean-square (rms) wave velocity, (d) salinity, and (e) suspended sediment concentration after a meteorological event (tides 5–8), following the same format as Fig. 3. Offshore wind velocity blowing from North to South in (c) is depicted with a dotted line.

to fetch, drag, water depth and variation in ocean swell) influence the average hourly wave climate.

These factors produce a time history of wave climate that often deviates significantly from the linear relationship. As shown in Fig. 6a, a decrease in wind velocity from 98 to 76 m^2/s^2 between $t = 13$ and 15 h (~23% decrease in energy) is correlated with a nonlinear decrease in the 20 min mean square wave energy from 0.051 to 0.028 m^2/s^2 (45% decrease in energy). Similarly, between hour 20 and hour 21, the wind velocity measured at the Richmond Field station was halved from 9.3 to 4.7 m/s. This sudden change in wind forcing causes a corresponding decline in the 20 min mean square energy of locally generated wind waves from a maximum of 0.06 m^2/s^2 (rms velocity of 0.24 m/s) to a maximum of 0.01 m^2/s^2 (rms velocity of 0.15 m/s) 2 h later (Fig. 6a). Though a linear model (e.g., Fig. 6c) predicts a factor 4 × decrease in wave energy, the actually measured wave energy decreases by a factor of 6 × . This greater than expected decrease suggests that other factors affect wave heights (e.g., water depth or tidal flow), and that variability in the wind-field at periods of less than 1 h may be important.

The sensitivity of wave energy to changes in wind climate is correspondingly reflected in the measured SSC (Fig. 6b). Increases in SSC concentration coincide with increases in wind energy (e.g., at $t = 11$ and 19 h), while decreases in SSC correlate with decreases in wind energy (e.g., at $t = 15$ and 30 h). During periods of onshore wind (data during the period of offshore wind from $t = 55$ to 88 h are omitted), the correlation between hourly averaged wind wave energy and hourly averaged SSC is $R^2 = 0.41$. When selected periods of anomalous SSC are removed (hours 19–21, 35–41 and 89), the correlation is increased to $R^2 = 0.58$ and a reasonably linear trend is observed (see Fig. 6d).

The sensitivity of the regression in Fig. 6d to omitting data and the scatter around the linear trend again points to the complexity and variability of the hydrodynamic forcing and sediment dynamics. However, because the correlation between tidal velocity and SSC is insignificant ($R^2 = 0.23$), other processes besides wind waves and tidal currents must control the variation of SSC (particularly during the times omitted in the analysis). These processes are the focus of the following sections (Sections 3.3 and 3.4).

Note that winds directed offshore (blowing from North to South) may also cause elevated SSC. For example, moderate offshore winds of 3–4 m/s during the ebb of tide 6 and flood of tide 7 produce negligible wind-wave energy (see Fig. 5) and hence no local erosion. However, the large SSC during the flood of tide 7 suggests that offshore wind is nonetheless important, as it likely produces waves and

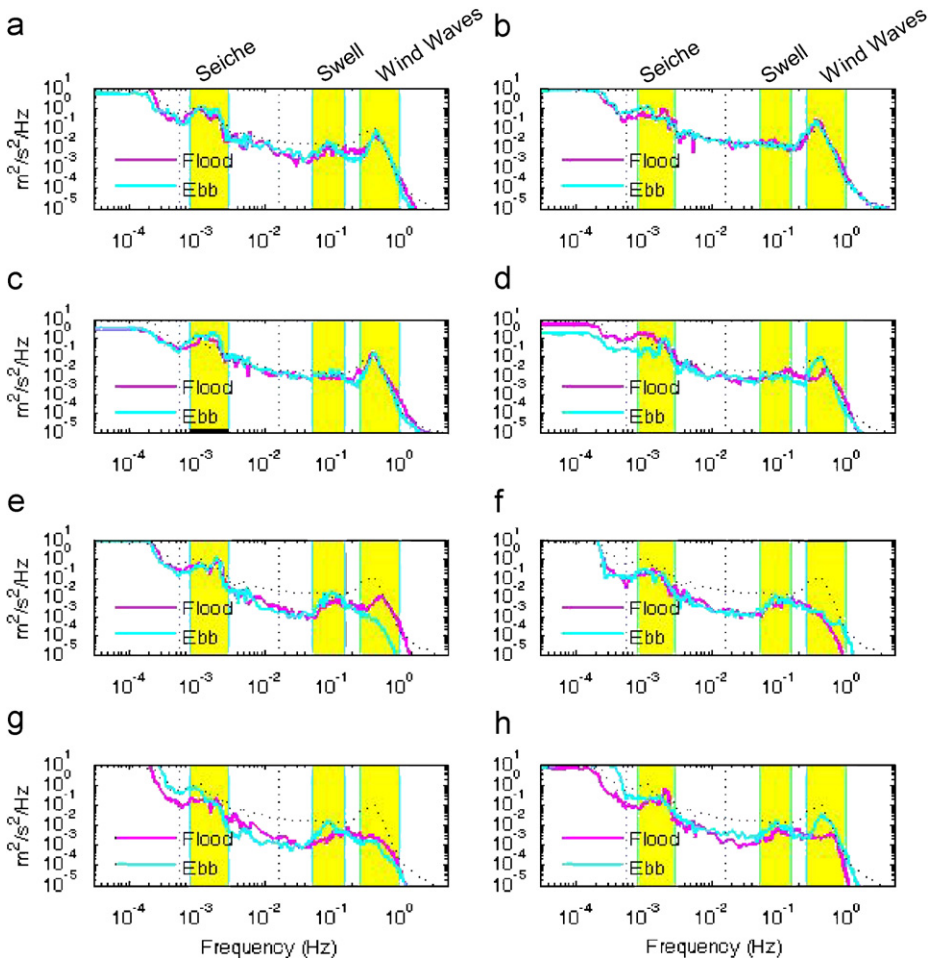

Fig. 5. Comparison of the power spectrum of velocity between flood (magenta, dark shade) and ebb (cyan, light shade) over eight tidal periods. The seiche, ocean swell, and wind wave frequency bands are shaded. For reference, the power spectrum during the ebb of tide 2 is presented as a dotted line. The vertical dotted lines refer to frequencies of 1/60 and 1/1800 Hz, and depict low energy frequencies used for averaging. (a) Tide 1, (b) tide 2, (c) tide 3, (d) tide 4, (e) tide 5, (f) tide 6, (g) tide 7, and (h) tide 8.

erosion in subtidal areas and results in a larger SSC signal than either the flood of tides 6 and 8, when offshore wind forcing is much smaller (see Fig. 4). By contrast, offshore winds during the ebb of tide 6 do not cause any erosion upstream (shoreward) of the instruments, and no significant increase in SSC occurs. Note that tidal velocities are slightly larger during the flood of tide 7 than either the flood of tide 6 or tide 8 (0.11 m/s vs. 0.07–0.08 m/s), and may also contribute to differences in offshore erosion and advection during these flood tides. Finally, ocean swell forcing is larger during the flood of tide 7 than during either the ebb of tide 7 or tide 8 (see Fig. 5), and may also contribute to differences in SSC.

3.3. Effect of seiching on SSC

To investigate the effect of seiching on SSC, we display the near-bed 1-min mean velocity and SSC between $t = 36.5$ and 40.5 h in Fig. 7a and b. Variations in velocity and SSC at a period of 500–1000 s occur through-out this period, and serve to increase the longer term mean SSC (e.g., tidal mean). Interestingly, a persistent asymmetry occurs between SSC and the phase of the seiche, with the largest sediment concentrations generally occurring when the seiche velocity is shoreward (shaded magenta, dark). This is clearly observed in the scatter plot of the 1-min mean velocity vs. the 1 min mean SSC (Fig. 8c) during this 4 h span. For mean, near-bed velocities less than −0.05 m/s, near-bed SSC is restricted to a narrow band around 0.1 kg/m^3. For velocities between −0.05 and 0.15 m/s, SSCs trend upwards from 0.1 kg/m^3 to as much as 0.5 kg/m^3.

Clearly, the stress exerted by the 1-min mean flow cannot explain the observed sediment concentration, since a mean velocity of zero m/s (mean stress = 0 N/m^2) results in larger sediment concentrations than an ebb velocity of 0.15 m/s. A possible explanation is that sediment is being resuspended by the ejection of sediment off of bedform ripples as the fluid reverses direction (e.g., Sleath and Wallbridge, 2002). Variation in the frequency of ejection over a seiche would then produce the observed behavior (Talke, 2005). Other explanations include settling lag effects or lateral interaction with turbid channel water.

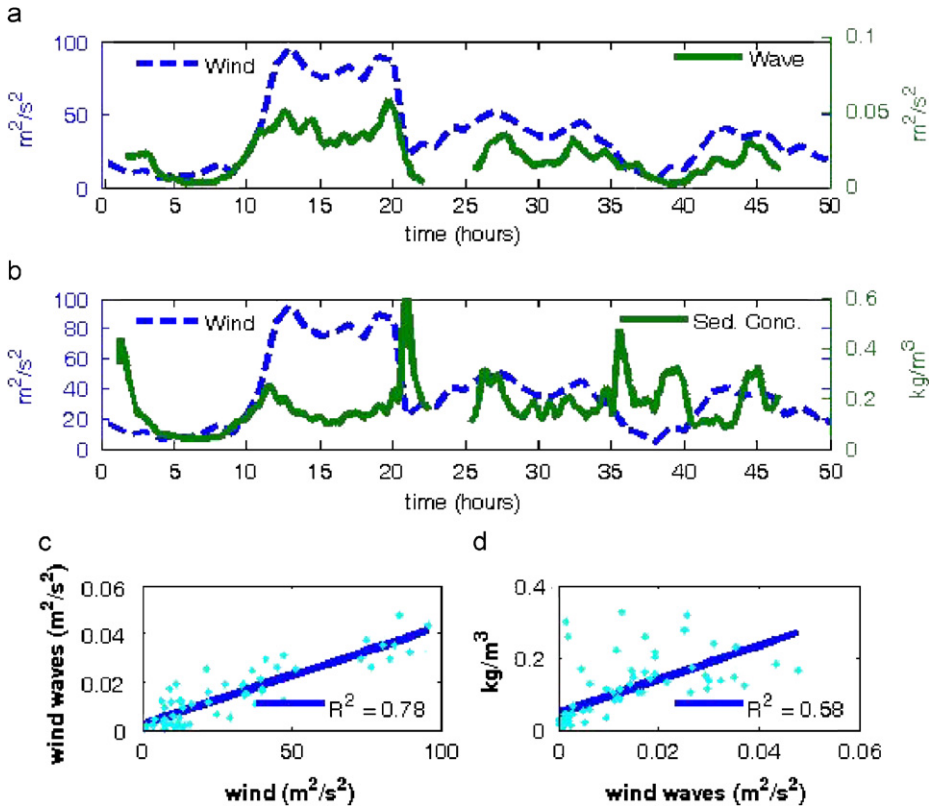

Fig. 6. Evolution of wind energy (a and b), wave energy (a) and sediment concentration (b) vs. time, and scatter plots of hourly averaged wind wave energy vs. wind energy (c) and hourly averaged suspended sediment concentration vs. the hourly averaged wind wave energy (d). The sediment concentration in (b) is a 30 min moving average. In (d), Sediment concentration measurements between hour 19–21, hour 35–41, and hour 89 are omitted because waves do not control sediment concentration values directly during this time. In addition, Wind energy between $t = 55$ and 88 h is omitted because it is blowing towards the south (i.e., offshore of the flat). Correlation of the line fit to data is given by the R^2 value.

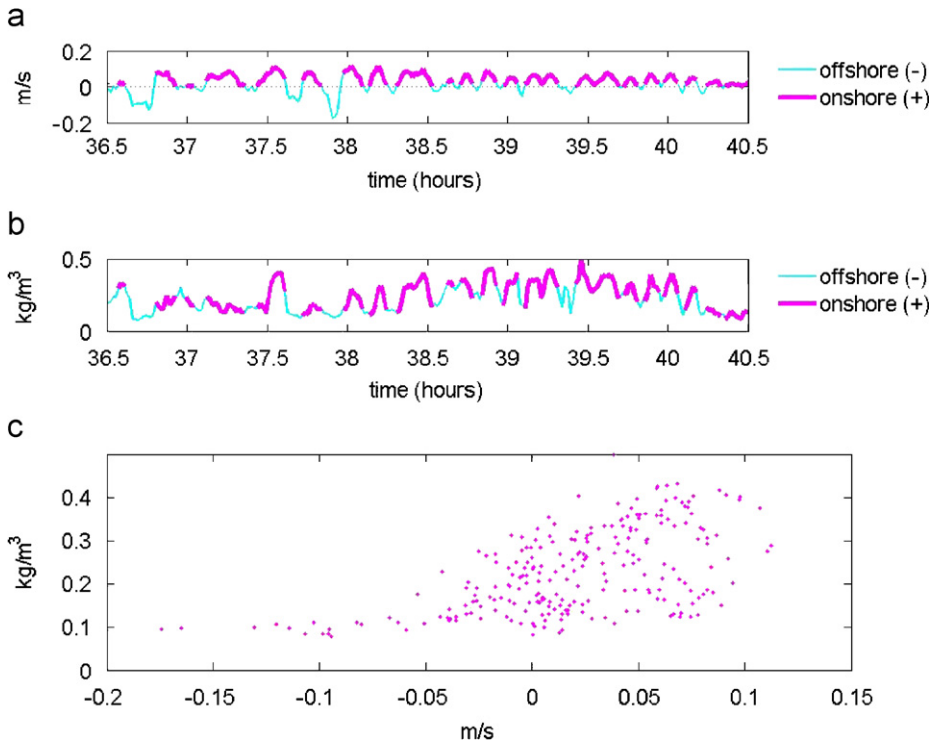

Fig. 7. Plot of the (a) 1 min mean velocity, (b) 1 min mean SSC, and a scatter plot (c) of 1 min mean SSC vs. 1 min mean velocity over the time period $t = 36.5$ to 40.5 h. Periods of onshore directed velocity are shaded magenta (dark) in (a) and (b). Measurements occurred at O(0.1 m) off the bed.

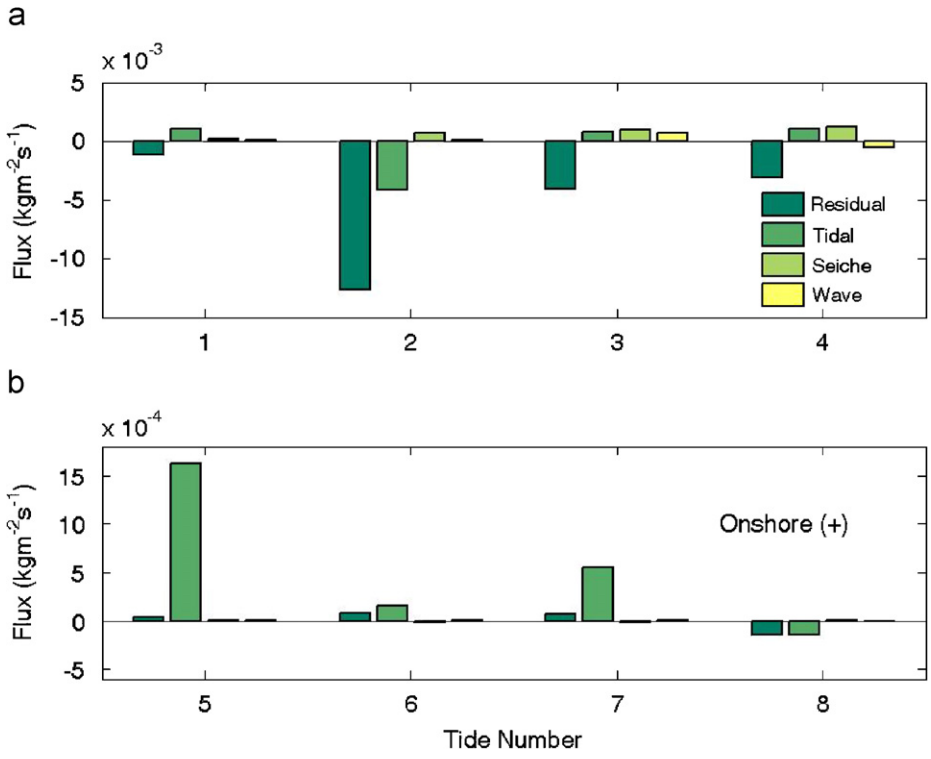

Fig. 8. Bar graph showing the sediment flux rates at four different time scales for tidal periods 1–8 (see Eqs. (1)–(7)). From left to right for a particular tidal period, the sediment flux rates depicted are at the residual (tidally averaged), tidally varying, seiching, and wave frequencies. The upper graph shows the tidal periods during a meteorological event characterized by sustained winds of up to 9 m/s, while the lower graph denotes tidal periods during the calmer period (wind speeds of 0–5 m/s) that follows. The onshore direction of flux is positive. *Y*-axis scale is different between tides 1–4 and tides 5–8.

3.4. Frontal processes

While elevated SSC is often correlated with local wave action (e.g., the range of times described in Fig. 6d, such as the flood of tide 5), examples of short duration (~30 min), high concentration events that are decoupled from the local wind climate occur during the ebb of tide 2 and the flood of tides 4, 6, and 8 (see Figs. 3 and 4). Such pulses of SSC, termed the 'turbid tidal edge', are often observed on tidal flats (Dyer et al., 2000) and are attributed to local erosion from tidal currents (e.g., Pritchard and Hogg, 2003). However, the small maximum tidal currents of 0.07–0.11 m/s during most of the experiment result in small shear stresses of 0.015–0.03 N/m^2 (using the quadratic friction law with a drag coefficient of 0.0025, an order of magnitude often found in coastal environments, e.g., Green and McCave, 1995) and used in models (e.g., Roberts et al., 2000), which are unlikely to cause local erosion. Moreover, the large rise in SSC often occurs as wind energy decreases (e.g., ebb of tide 2 and flood of tide 4), and hence does not follow the linear relationship suggested between SSC and wind (Fig. 6). In the absence of wind forcing, the turbid tidal edge still occurs, despite the minimal local forcing (e.g., flood of tides 6 and 8).

A common feature of all the turbid pulses is that they coincide with sharp rises or falls in salinity. Using the approximation that $ds/dx \sim ds/dt/U$ (where s is the salinity and U is the tidal velocity), we estimate that the turbid pulse ($>0.9\,kg/m^3$) and salinity decrease (22.5 to ~1 psu) between hour 20 and hour 21 coincides with salinity gradients of ~40 psu/km and that the rise in turbidity (from 0.3 to 0.52 kg/m^3) and salinity (+9.4 psu) at $t = 26.25$ h over a 2 min span implies a local gradient of ~800 psu/km. During the calmer periods of tides 6 and 8, gradients of ~0.030 and 0.01 psu/m are advected past the sensors and coincide with a factor ~5× increase in SSC (peak of 0.13 and 0.2 kg/m^3, respectively). Salinity gradients are larger during the flood, and are consistent with values observed in the nearby subtidal channel by Ralston and Stacey (2005).

The sharp variations in sediment concentration and salinity observed during ebbing and flooding periods suggests that a front influenced by freshwater runoff is moving past the sensors. The pulse of SSC observed during the ebb of tide 2 and the flood of tides 3, 4, 6, and 8 is consistent with a turbidity maximum formed at the interface of two bodies of water in which longitudinal mixing is suppressed by strong horizontal density gradients. This mechanism is described for the nearby channels by Ralston and Stacey (2005), and our data suggest this process also occurs on the adjoining flats. The SSC in a front likely consists of sediment eroded non-locally during the previous tidal period or at offshore (more energetic) locations, and held in suspension by settling lag and turbulence effects (Ralston and Stacey, 2007). Frontal processes govern the formation, dispersion, and time scale

of the pulses of SSC. While Ralston and Stacey (2005, 2007) describe a process occurring primarily during flood tides after Low–Low-Water (LLW), our data suggest frontal processes can occur during the ebb (e.g., tide 2) and after High–Low-Water (HLW) given sufficient freshwater discharge (e.g., tide 6).

3.5. Sediment fluxes

In this section we investigate the sediment flux occurring over a tide at different time scales. Combining the effect of locally driven wind waves and ocean swell together, we split the measured velocity $V(t)$ and sediment concentration $C(t)$ into wave, seiche, tidal, and residual (tidally averaged) components,

$$C = C_{residual} + C_{tide} + C_{seiche} + C_{wave}, \quad (1)$$

$$V = V_{residual} + V_{tide} + V_{seiche} + V_{wave}. \quad (2)$$

Velocity is decomposed along the North–South axis, which corresponds to the down-slope direction and the primary direction of both wave and tidal forcing. Using the function f for either the measured sediment concentration, C, or velocity, V, we decompose the measured signal using bin-averages over the time scales T, N, and M,

$$f_{residual} = \frac{1}{T}\sum_{t=0}^{t=T} f(t)\,\Delta t, \quad (3)$$

$$f_{tidal}(t)|_{t=N(i-1)}^{t=iN-\Delta t} = \frac{1}{N}\sum_{t=N(i-1)}^{t=iN} (f(t) - f_{residual})\,\Delta t, \quad i = 1,2,\ldots,\frac{T}{N}, \quad (4)$$

$$f_{seiche}(t)|_{t=j(M-1)}^{t=jM-\Delta t} = \frac{1}{M}\sum_{t=j(M-1)}^{t=jM} (f(t) - f_{residual} - f_{tidal})\,\Delta t, \quad j = 1,2,\ldots,\frac{T}{M}, \quad (5)$$

$$f_{wave}(t) = f(t) - f_{residual} - f_{tidal} - f_{seiche}. \quad (6)$$

The time increment Δt is the sampling period of 1/8 s. These decompositions result in histograms of velocity and SSC with time increments of T, N, or M (Eqs. (3), (4), and (5), respectively). The residual time scale for an intertidal flat is the time of immersion, T, which we estimate as an integer number of 10 min measurement bursts. We define the tidally varying time scale N to be 1800 s (30 min), and the variability of the seiche scale M to be 60 s (1 min). These time scales correspond to periods of low energy in the power spectrum of velocity, as defined by the frequencies 1/1800 and 1/60 Hz in Fig. 5. While some unsteadiness from lower frequencies is contained in higher frequency components (e.g., the tidal signal varies somewhat over 30 min and enters f_{seiche}), this variability is small compared to the higher frequency variability (e.g., the seiche). Note that the number T/N is rounded up to the nearest integer. When T/N is not an integer number, the averaging time of the last bin is defined by the time period of the remainder. In practice, this means that N is equal to 10 or 20 min for the last bin in some tidal periods, and may result in some truncation of the seiche signal.

Assuming that diffusive fluxes are small, the average sediment flux $\Phi_{SSC} = (1/T)\int_0^T CV\,dt$ over a period of immersion T at one point in the water column is then:

$$\Phi_{SSC} = \frac{1}{T}\int_0^T (C_{wave}V_{wave} + C_{seiche}V_{seiche} + C_{tidal}V_{tidal} + C_{residual}V_{residual} + \Phi_{cross-terms})\,dt \quad (7)$$

The cross-terms are extremely small when integrated over the time period T, and are typically less than $10^{-12}\,kg\,m^{-2}\,s^{-1}$ (see the electronic supplement for additional discussion).

The sediment fluxes occurring during tides 1–4 and tides 5–8 are shown in Fig. 8a and b. Positive values of flux denote onshore transport, while differences in y-axis scaling between Fig. 6a and b reflect the order of magnitude larger fluxes during tides 1–4. The tidally averaged, residual flux of sediment $(1/T)\int_0^T C_{residual}V_{residual}\,dt$, is directed offshore during tides 1–4 (average of $-5.4\times10^{-3}\,kg/m^2/s$) but nearly vanishes during tides 5–8 ($6.5\times10^{-6}\,kg/m^2/s$). Flux from tidally varying processes, $(1/T)\int_0^T C_{tidal}V_{tidal}\,dt$, is offshore during tides 1–4 (average of $-4.0\cdot10^{-4}\,kg/m^2/s$) and onto the flat for tides 5–8 ($5.5\times10^{-4}\,kg/m^2/s$). The flux of SSC at the seiching frequency, $(1/T)\int_0^T C_{seiche}V_{seiche}\,dt$, is always directed onshore, and accounts for 14% of the total flux during tides 1–4, but less than 1% of the flux during tides 5–8. Fluxes at the wave frequency ($<1/60$ Hz) are small but non-negligible during tides 3–4. Because no coherence is observed in the optical backscatter signal at wind-wave frequencies, these fluxes may reflect transport due to lower frequency variability such as ocean swell or wind-wave groups.

Overall, tidally averaged, residual processes dominate net export of sediment during the meteorological event of tides 1–4 (i.e., $\int_0^T CV\,dt<0$) and tidally varying processes produce onshore flux during the calmer period of tides 5–8 (i.e., $\int_0^T CV\,dt>0$). Offshore sediment fluxes during the meteorological event (tides 1–4) are an order of magnitude larger than the onshore fluxes during the calmer period immediately afterwards (tides 5–8).

4. Discussion

In this section we discuss the physical mechanisms that produce fluxes during both the meteorological event and afterwards.

4.1. Residual, tidally averaged fluxes

The dominance of tidally averaged, residual fluxes during tides 1–4 is caused by order of magnitude increase in $C_{residual}$ and $V_{residual}$ above non-event conditions

(e.g., tides 5–8). Fig. 9 shows that during the meteorological event, residual flow off the flat increases from ~−0.01 m/s at the beginning of the meteorological event (tide 1) to a maximum of −0.075 m/s during tide 2. By comparison, the tidally averaged velocities after the meteorological event vary from 0.001 to 0.008 m/s. Similarly, tidally averaged sediment concentrations during the meteorological event (0.11–0.19 kg/m^3) are much larger than sediment concentrations afterwards (0.02–0.05 kg/m^3). The combination of elevated sediment concentrations and increased residual flows causes large fluxes of sediment off the flat, particularly for tides 2, 3, and 4. During the calm period after the meteorological event, tidally averaged fluxes are correspondingly decreased; moreover, because the direction of flux is positive during tides 5 and 7 but negative during tides 6 and 8, the integrated net flux over the post-event period is further reduced.

During the meteorological event between April 11 and 13, many factors may work together to create the residual flow pattern. The large salinity variations observed during this time period (see Fig. 3) indicate an influence of freshwater runoff from the local water shed. Wind stress also produces circulation patterns, as evidenced by water level set-up and its release during tides 1–5. The large salinity gradients likely drive gravitational circulation, which was found by Ralston and Stacey (2005) to produce a near-bottom inflow on the order of 0.01–0.02 m/s over the shoal of our experimental site. Finally, the diurnal inequality in water level that occurs during tides 1–4 results in residual, tidally averaged currents.

The tidally averaged increase in SSC during tides 1–4 is primarily a result of the increased wave forcing, as suggested by the regressions in Fig. 6. However, seiching motions also appear to drive increases in tidally averaged SSC (see Section 3.3). The more rigorous mixing during periods of large wind waves also keeps sediments in suspension during slack tides, hence reducing the deposition (removal) of sediments. Combined with the offshore flow of water near the bed, sediment is exported from the flat to deeper offshore waters.

4.2. Tidal time scale

Sediment flux due to tidally varying processes is controlled by asymmetries in SSC and velocity over a tidal period. We investigate the factors influencing net flux at the tidal time scale by decomposing the SSC and velocity measurements into symmetric and asymmetric components

$$C_{tidal} = C_{base} + C', \tag{8a}$$

$$V_{tidal} = V_{base} + V', \tag{8b}$$

where C_{base} is an even (symmetric) function and V_{base} is an odd function with respect to the midpoint of the period of immersion ($T/2$), and C' and V' are deviations from the symmetrical function over the tidal period. Using our data, we define the even component of SSC around $T/2$ as follows:

$$C_{base}(t) = C_{tidal}(t), \quad t < \frac{T}{2}, \tag{9}$$

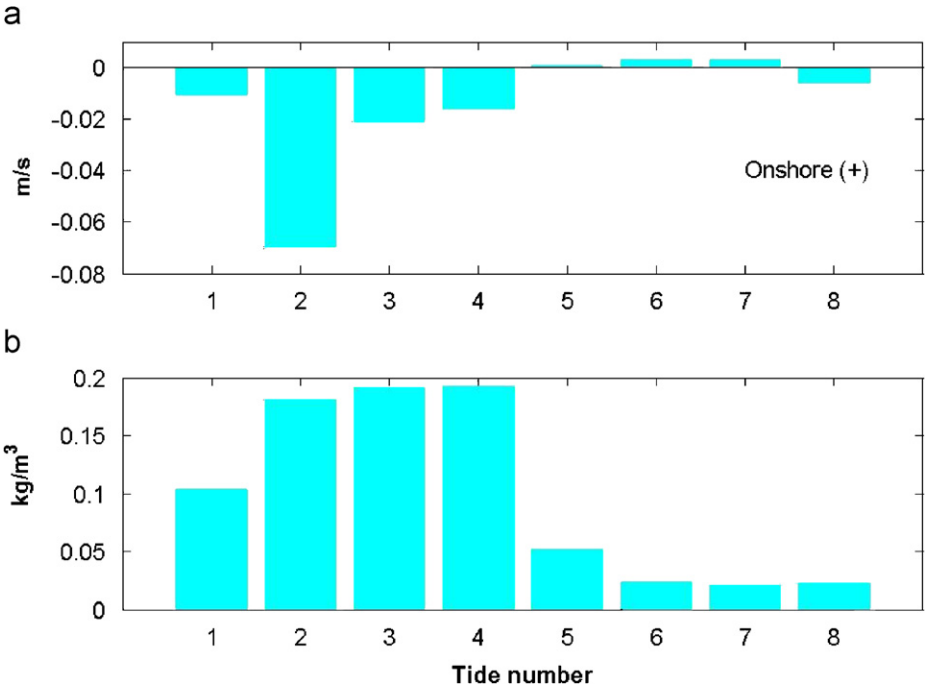

Fig. 9. Residual, tidally averaged velocity (a) and suspended sediment concentration (b) over the eight tidal periods of the experiment. Tides 1–4 occur during a meteorological event characterized by rainfall and sustained winds of up to 9 m/s. The remaining tides (5–8) occur during a calmer, dry period with winds of 0–5 m/s.

$$C_{base}(t) = C_{tidal}(T-t), \quad t > \frac{T}{2}.$$

The odd component of velocity is defined similarly:

$$V_{base}(t) = V_{tidal}(t), \quad t < \frac{T}{2}, \tag{10}$$

$$V_{base}(t) = -V_{tidal}(T-t), \quad t > \frac{T}{2}.$$

Using these definitions, we find that the tidally integrated flux of SSC at the tidal time scale can be rewritten as,

$$\frac{1}{T}\int_0^T C_{tidal}V_{tidal}\mathrm{d}t = \underbrace{\frac{1}{T}\int_0^T C_{tidal}V'\mathrm{d}t}_{\Phi_{V'}} + \underbrace{\frac{1}{T}\int_0^T V_{base}C'\mathrm{d}t}_{\Phi_{C'}} \tag{11}$$

where we have used the observation that the integral of the product of even and odd functions vanishes over the time period T, i.e., $\int_0^T (C_{base}V_{base})\,\mathrm{d}t = 0$. Hence, asymmetries in velocity (V') and SSC (C') over a tidal period are required to produce sediment fluxes $\Phi_{V'}$ and $\Phi_{C'}$, respectively (see Eq. (11)).

Fig. 10 shows the magnitude of the sediment fluxes $\Phi_{V'}$ and $\Phi_{C'}$ over tides 1–8. During tides 1–3, both components of flux are on the same order of magnitude. By contrast, the $\Phi_{V'}$ term nearly vanishes during tides 5–8 and the tidally varying fluxes are dominated by asymmetries in SSC between the flood and the ebb.

To understand why the shift to $\Phi_{C'}$ dominance occurs in tides 5–8, we investigate the tidal variation of SSC (Figs. 11a and 12a), velocity (Figs. 11b and 12b) and the product $C_{tidal}V_{tidal}$ (Figs. 11c and 12c) during tides 1–4 (Fig. 11) and tides 5–8 (Fig. 12). Onshore velocity and sediment flux are shaded dark (magenta) and defined as (+), whereas offshore sediment flux and velocity are shaded light (cyan) and defined as (−). Similarly, positive deviations from the tidal averaged SSC are shaded dark (+) and negative deviations are shaded light and defined as (−) (see Eq. (5)). The function C_{base} is depicted in Figs. 11a and 12a and the function V_{base} is depicted in Figs. 11b and 12b.

During the meteorological event, both SSC and velocity are quite asymmetric, as can be observed by the differences between the measured tidal variation (C_{tidal} and V_{tidal}) and the hypothetical symmetric functions C_{base} and V_{base}. While SSC remains asymmetric over a tidal period during tides 5–8, the flow velocity is relatively symmetric (as shown by the relatively good agreement between V_{base} and V_{tidal}).

4.2.1. Factors producing asymmetry

The asymmetric tidal variation in flow velocity during the meteorological event, V', is caused both by the diurnal inequality in tides and by events such as freshwater discharge and wind-induced circulation and set-up/set-down. For example, the diurnal inequality results in small tidal currents during the ebb of tide 1 and flood of tide 2, and contributes to an onshore $\Phi_{V'}$ during tide 1 and an offshore $\Phi_{V'}$ during tide 2 (see Fig. 10). The set-up caused by wind also appears to prolong the flood tide during tide 2. Finally, the coincidence of freshwater discharge (as evidenced by salinity concentrations <10 psu) and the release of water set-up due to decreasing wind at hour 20 cause

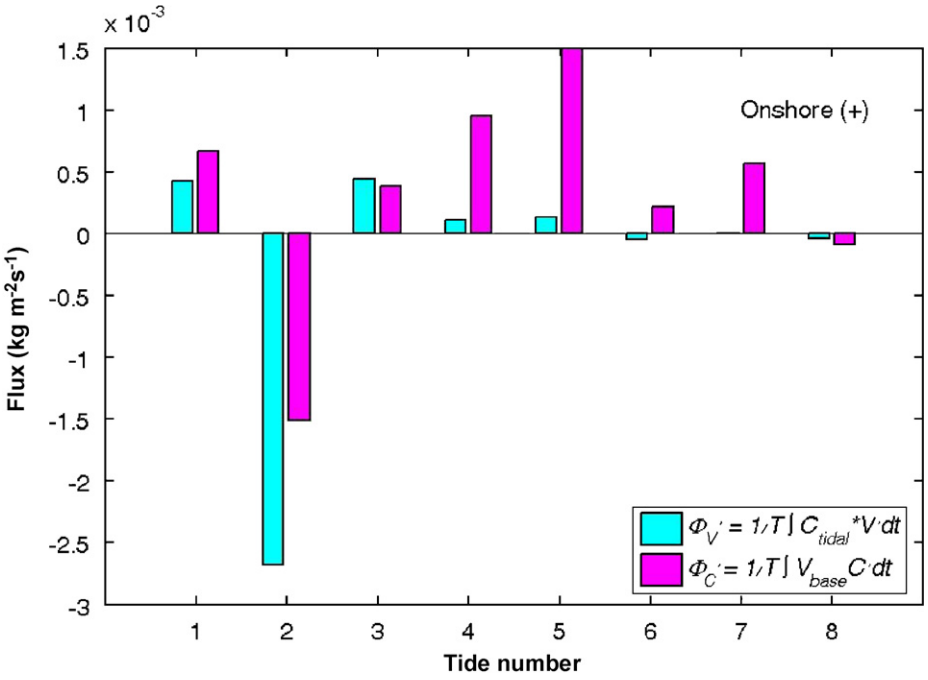

Fig. 10. Comparison of tidally integrated sediment flux caused by asymmetries over a tidal cycle in tidally varying velocity ($\Phi_{V'}$) and SSC ($\Phi_{C'}$), as defined in equation. Tidal periods 1–4 coincided with a meteorological event with sustained wind speeds of up to 9 m/s, while tides 5–8 occurred in the calmer period that followed (winds of 0–5 m/s).

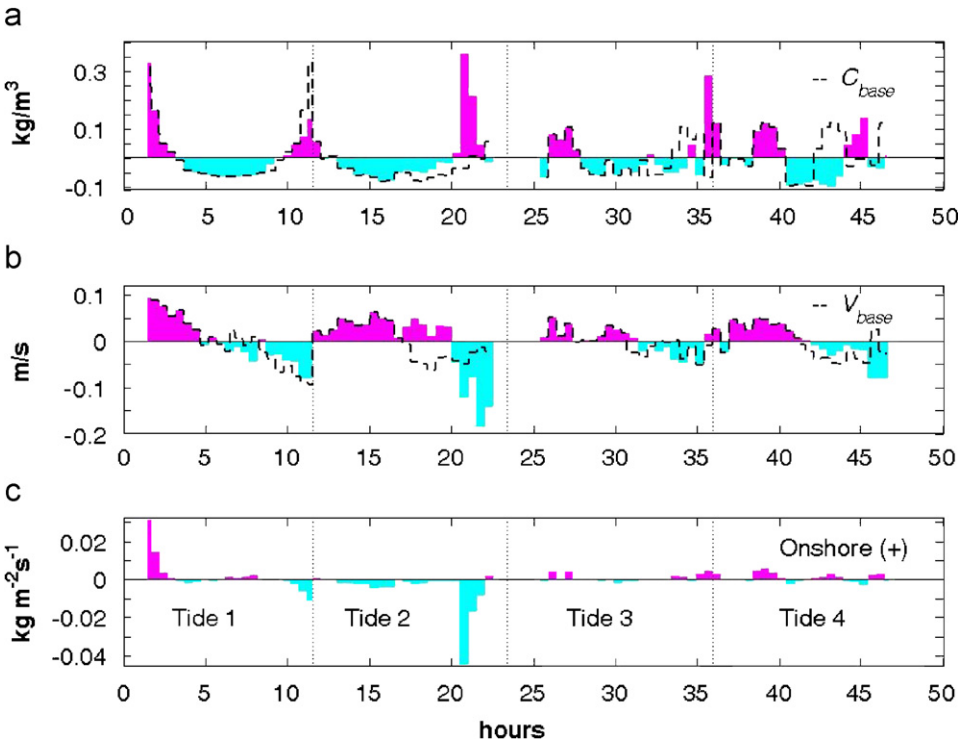

Fig. 11. Tidal component of (a) suspended sediment concentration, (b) velocity, and (c) suspended sediment flux for tides 1–4, constructed using the 30 min average (Eq. (5)). Sediment concentrations and velocities are deviations from the tidal average. SSC and velocity components larger than the tidal mean are dark colored (majenta), while components less than the tidal mean are shaded light (cyan). Around $T/2$ for each tidal period, an even symmetrical function, C_{base}, has been constructed for SSC (dashed line in (a) and an odd function, V_{base}, has been constructed for velocity (dashed line in (b). The vertical dotted line delineates tidal boundaries.

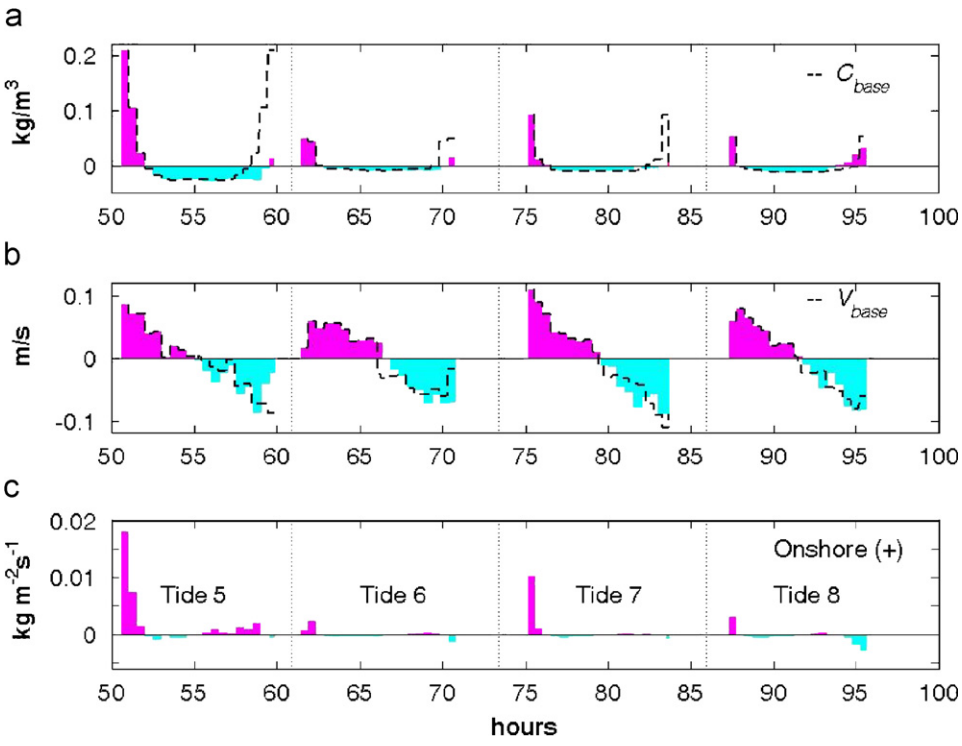

Fig. 12. Tidal component of (a) suspended sediment concentration, (b) velocity, and (c) suspended sediment flux for tides 5–8, following the same format as Fig. 11.

large ebb currents. As the diurnal inequality diminishes and the freshwater discharge and set-up disappear (particularly after tide 5), the asymmetric velocity profile becomes unimportant to the flux balance. Hence, unlike modeling studies suggest (e.g., Ridderinkhof, 1998), asymmetries in velocity caused by over-tides (e.g., the M_4 tide) do not appear to be important for fluxes at our site.

Two primary forcing mechanisms produce asymmetries of SSC over a tidal cycle at our site: The turbid tidal edge (mediated by frontal processes) and the tidal variation in wind forcing. In the absence of significant wind or wave activity (e.g., tide 6), the baseline asymmetry in SSC is characterized by higher concentrations on flood tides than on ebbs due to the turbid tidal front. These frontal pulses of turbidity are associated with strong salinity gradients, occur over a short time scale ($\ll 1$ h), and are usually largest during the flood tide (see Section 3.4). Variations in wind forcing cause tidal variations in wind-wave energy and seiching (see Fig. 5) over time scales greater than an hour, and hence alter SSC (see Sections 3.2 and 3.3).

The tidal asymmetry in SSC due to wind forcing is most clearly observed by comparing tides 5 and 8. During the flood of tide 5, wind-driven waves produce a peak concentration of $\sim 0.2\,kg/m^3$ above the tidal mean, which reduces over 1.5 h as wind forcing subsides (see Figs. 4 and 12). Because wind-wave energy is negligible during the ebb (see Fig. 5), SSC does not increase much and a flood dominated SSC asymmetry (and onshore sediment flux) occurs. By contrast, wind energy and wave energy are small during the flood of tide 8, but increase during the ebb (see Figs. 4 and 5). As a result, SSC shifts above the tidal average for 1.5 h during the ebb of tide 8, producing a net offshore flux.

The effect of variable wind forcing on asymmetries in SSC is not solely tied to local variations in wind-driven waves. For example, seiching motions are much larger during the flood of tide 4 than during the ebb, likely due to the decrease in wind forcing (and release of set-up) that occurs after hour 33 (see Figs. 3 and 5). These seiching motions not only increase the magnitude of SSC at the seiche frequency (see Fig. 7), but also increase the tidally varying SSC (e.g., between hours 38 and 40 in Fig. 11). Similarly, the decrease in wind during the ebb of tide 2 is correlated with large ebb currents that can erode sediment. Offshore (southwards directed) wind may stir offshore, subtidal sediments (through wave action) which are transported shoreward during the flood, and cause a flood dominated asymmetry in SSC over a tidal period (e.g., tide 7; see Section 3.2). Finally, ocean swell forcing is larger during the ebb of tide 5 and the flood of tide 7 than the corresponding flood and ebb, respectively, and may also contribute to asymmetries in SSC.

4.2.2. Effects of phasing and time scales

The net effect of asymmetries in velocity (V') and SSC (C') depends on their relative phasing with C_{tidal} and V_{base} and on their respective magnitudes and time scales of variation. Instantaneous fluxes of SSC at the tidal time scale are maximized when large SSC is correlated with large advective velocities. As shown in Figs. 11 and 12, examples of such events are found during the ebb of tide 2 (hour 20) and the flood of tide 1 (hour 2) and 5 (hours 51–53). Much smaller fluxes, however, occur when large SSC corresponds with small tidal velocities (e.g., hour 35), or when maximum tidal velocities occur at small SSC (hour 70 or hour 84).

Because of differing time scales and timing, turbid tidal fronts and wave-induced turbidity events interact differently with V_{base} in Eq. (11). Turbid pulses during the flood are often higher in magnitude than the corresponding increase in SSC during the ebb (see tides 6 and 8 in Fig. 12), and drive onshore flux in calm conditions (e.g., tide 6). However, the time scale over which the turbid pulse acts is small ($\sim$30 min) compared to wave-induced turbidity events, which generally occur over time periods of greater than 1 h (see flood of tide 5 and ebb of tide 8, for example). Hence, fluxes from the relatively small SSC during the ebb of tide 8 (Fig. 12), which is integrated over 1.5 h, outweighs the short but intense turbidity front which is integrated over 30 min. The effect of the differing time scales is amplified by the timing of the front and the wind event. The front during the flood of tide 8 occurs at a non-peak flood velocity (0.053 m/s vs. 0.083 m/s at the maximum), while the much smaller maximum SSC during the ebb of $0.08\,kg/m^3$ occurs at the nearly the maximum ebb velocity (0.081 m/s). Because wind events are longer, they are more likely to coincide with the maximum tidal velocity and therefore produce large sediment fluxes.

4.3. Time scales of wind and swell

As observed in the previous section, the timing of wind events relative to the phase of the tide modifies the net flux onto or off of the flat. Two basic conditions may occur. First, the wind wave event may last over the entire tidal period, as occurs during most of tide 2 during the meteorological event. On the other extreme, wind events may occur entirely during the flood (tide 5) or during the ebb (tide 8). To understand the likelihood that a wind event will be biased towards either the flood or ebb, we analyze wind data from the Richmond Field Station for the years 1999–2005. We define an event to be the time period over which sustained winds are greater than 5 m/s, which is a standard deviation from the long-term mean of 3.2 m/s and is also the order of magnitude for which sediment resuspension occurs on other intertidal flats (de Jonge and van Beusekom, 1995; Christie et al., 1999; Dyer et al., 2000). Two events that are separated by only 1 h are combined into one event period, to allow for randomness in the wind field during a contiguous event. For comparison, we also analyze the significant wave height (average of top 1/3 measured wave amplitudes per hour) measured at an offshore buoy (NDBC buoy 46026) for an

estimate of offshore swell. Again, we define an event as a standard deviation from the average, which is 2.8 m (mean significant wave height = 2.0 m). Though ocean swell rarely dominates the energy budget at this site, Fig. 5 shows that ocean swell provides an important contribution to the total forcing. Thus, the time scales of ocean swell provide an interesting contrast to locally driven wind waves.

Results in Fig. 13 show that the most likely time scale of both a wind event and ocean swell event is 1 h (26% and 28%, respectively). Thus, as confirmed by the spectral analysis of velocity (see Fig. 5), both ocean swell and wind waves are highly likely to occur over only a portion of the tide: ~51% of wind events are 3 h or less, while ~54% of offshore swell events are 5 h or less. Indeed, 90% of wind events have a time period of less than 12 h, the time scale of a tide. By contrast, 28% of offshore swell events exceed the time scale of a tidal period.

The frequency distribution of wind and ocean swell events suggests that the strong dependence of tidally integrated sediment flux to variations in wind and waves are a long-term characteristic of this intertidal flat, and not just an artefact of this experiment. Changes in wind forcing and hence sediment flux are observed both within a tidal phase (e.g., during the ebb of tide 2 between hours 20 and 21) and between tidal phases (e.g., the flood and ebb of tide 5 or tide 8). As a result, the phasing and duration of wind and wave events relative to the local tidal forcing is an important factor in the net sediment flux. Hence, the assumption that wind forcing is constant over a tidal period in models of sediment transport (e.g., Ridderinkhof, 1998; Roberts et al., 2000; Waeles et al., 2004), may need to be examined.

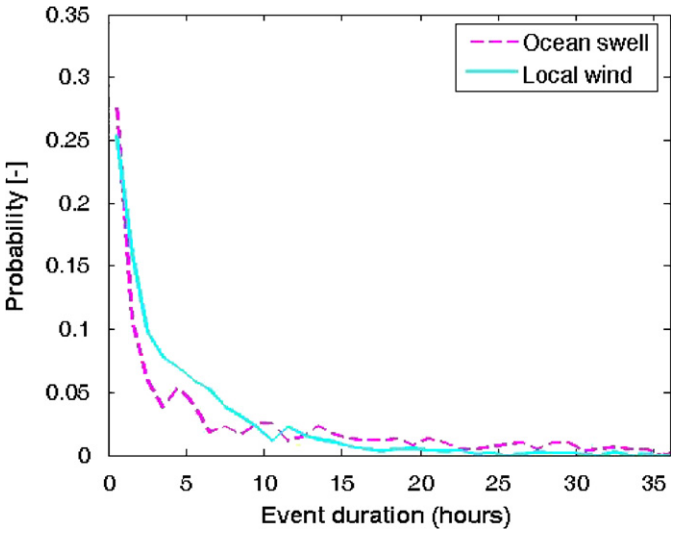

Fig. 13. Probability distribution of event length for offshore waves and local wind defined from 6 years of data (1999–2005). An event is defined as an offshore wave height exceeding 2.78 m and a wind speed exceeding 5 m/s, which represents any measurement greater than a standard deviation from the mean. The number of consecutive measurements that exceed the event threshold determines the time scale of the event. Over half (51%) of wind events occur over a time period of 3 h or less, and over half (54%) of ocean swell events occur over a time period of 5 h or less. Only 10% of wind events, but 28% of offshore wave events, exceed 12 h of duration.

5. Conclusions

Field observations of hydrographic parameters and sediment concentration on an intertidal flat show that multiple frequencies of forcing contribute to the flow field, including locally driven wind waves, ocean swell, intra-tidal seiching motions (500–1000 s period), tidal flows, and sub-tidal variation such as freshwater discharge. Because the median time scale of wind and swell events is small (3 and 5 h, respectively), wave and seiching motions (and hence SSC) are often asymmetrically distributed between ebb and flood. Precipitation from a meteorological event leads to freshening and the formation of a sharp salinity front that is advected past the sensors during the flood and ebb. Sediment is trapped at the salinity front, and is observed at the sensors as a short (~30 min) but intense increase in SSC.

Sediment is exported during a meteorological event primarily due to wind driven and freshwater forcing. Tidally averaged fluxes of SSC dominate and are marked by an order of magnitude increase in both the residual circulation (offshore) and tidally averaged sediment concentration. The enhanced residual circulation is likely driven by wind and freshwater forcing, while increases in SSC are primarily driven by local wind waves and seiching. Tidally varying processes (such as wind forcing and frontal dynamics) either amplify (tide 2) or diminish (tide 4) the net sediment fluxes during the meteorological event by producing asymmetries in both the tidal velocity and the tidal profile of SSC. Net sediment fluxes at the seiche frequency are always onshore due to a bias in SSC with respect to the seiche period, and occur primarily during the meteorological event.

After the meteorological event, both tidally averaged wind and freshwater forcing relax and the dominant contribution to sediment flux is made by tidally varying processes. In particular, the flood tide is marked by elevated turbid fronts, both from onshore wind (tide 5), offshore wind (tide 7) and salinity driven frontal processes (tides 6 and 8). By contrast, salinity decreases more gradually during the ebb and little erosion or trapping of SSC occurs. As a result of this asymmetry in SSC, sediment flux is generally onshore. However, moderate onshore wind of 3–4 m/s during an ebb period (e.g., tide 8) is capable of producing significant increases to SSC and reversing the net sediment flux.

To conclude, sediment fluxes at an intertidal flat are controlled by periodic tidal forcing and by event driven processes such as wind and freshwater discharge. The shifting influence of wind and freshwater discharge over a period of days produces large, tidally averaged fluxes during a meteorological event and produces the asymmetries necessary for sediment transport at a tidal frequency. Over the time period considered, the phasing and duration of wind events and freshwater discharge relative to the local tidal forcing greatly affect net sediment flux.

Acknowledgments

Many thanks to David Ralston, Jon Fram, Deanna Sereno, Seungjin Baek, Shitao Xu, Kate Hucklebridge, Josh Sharp, and Kurt Talke for logistical support during the experiment. The research was funded by National Institutes of Health grant number P42ES0475 from the National Institute of Environmental Health Sciences, and was completed with the funding of LOICZ project 014.27.013 (Land Ocean Interaction in the Coastal Zone, funded by NWO-ALW, the Netherlands Organization for Scientific Research). The authors thank the anonymous reviewers for their helpful and constructive criticism.

Appendix A. Supplementary materials

Supplementary data associated with this article can be found in the online version at doi:10.1016/j.csr.2007.12.003.

References

Andersen, T.J., Pejrup, M., 2001. Suspended sediment transport on a temperate, microtidal mudflat, the Danish Wadden Sea. Marine Geology 173, 69–85.

Bassoullet, P., Hir, P.L., Gouleau, D., Robert, S., 2000. Sediment transport over an intertidal mudflat: field investigations and estimation of fluxes within the 'Baie de Marennes-Oleron' (France). Continental Shelf Research 20, 1635–1653.

Black, K.S., 1998. Suspended sediment dynamics and bed erosion in the high shore mudflat region of the Humber Estuary, UK. Marine Pollution Bulletin 37 (3–7), 122–133.

Christiansen, C., Vølund, G., Lund-Hansen, L.C., Bartholdy, J., 2006. Wind influence on tidal flat sediment dynamics: field investigations in the Ho Bugt, Danish Wadden Sea. Marine Geology 235, 75–86.

Christie, M.C., Dyer, K.R., Turner, P., 1999. Sediment flux and bed level measurements from a macro tidal mudflat. Estuarine, Coastal and Shelf Science 49, 667–688.

de Haas, H., Eisma, D., 1993. Suspended-sediment transport in the Dollard estuary. Netherlands Journal of Sea Research 31 (1), 37–42.

de Jonge, V.N., van Beusekom, J.E.E., 1995. Wind and tide induced resuspension of sediment and microphytobenthos from tidal flats in the Ems estuary. Limnology and Oceanography 40, 766–778.

Dyer, K.R., 1998. The typology of intertidal mudflats. In: Black, K.S., Patterson, D.M., Cramp, A. (Eds.), Sedimentary Processes in the Intertidal Zone. Geological Society, vol. 139. Special Publications, Londons, pp. 11–24.

Dyer, K.R., Christie, M.C., Feates, N., Fennessy, M.J., Pejrup, M., van der Lee, W., 2000. An Investigation into processes influencing the morphodynamics of an intertidal mudflat, the Dollard Estuary, The Netherlands: I. Hydrodynamics and suspended sediment. Estuarine, Coastal and Shelf Science 50, 607–625.

Friedrichs, C.T., Aubrey, D.G., 1996. Uniform bottom shear stress and equilibrium hypsometry of intertidal flats. In: Pattiaratchi, C. (Ed.), Coastal and Estuarine Studies, vol. 50. American Geophysical Union, pp. 405–429.

Green, M.O., McCave, I.N., 1995. Seabed drag coefficient under tidal currents in the eastern Irish Sea. Journal of Geophysical Research 100 (C8), 16057–16070.

Janssen-Stelder, B., 2000. The effect of different hydrodynamic conditions on the morphodynamics of a tidal mudflat in the Dutch Wadden Sea. Continental Shelf Research 20, 1461–1478.

Kirby, R., 2000. Practical implications of tidal flat shape. Continental Shelf Research 20, 1061–1077.

Kornman, B.A., de Deckere, E.M.G.T., 1998. Temporal variation in sediment erodibility and suspended sediment dynamics in the Dollard estuary. In: Black, K.S., Paterson, D.M., Cramp, A. (Eds.), Sedimentary Processes in the Intertidal Zone, vol. 139. Special Publications, Geological Society, London, pp. 231–241.

Le Hir, P., Roberts, W., Cazaillet, O., Christie, M., Bassoullet, P., Bacher, C., 2000. Characterization of intertidal flat hydrodynamics. Continental Shelf Research 20, 1433–1459.

O'Brien, D.J., Whitehouse, R.J.S., Cramp, A., 2000. The cyclic development of a macrotidal mudflat on varying timescales. Continental Shelf Research 20, 1593–1619.

Pritchard, D., Hogg, A.J., 2003. Cross-shore sediment transport and the equilibrium morphology of mudflats under tidal currents. Journal of Geophysical Research 108 (C10), 2003–3313 (doi:10.129/2002JC001570).

Pritchard, D., Hogg, A.J., Roberts, W., 2002. Morphological modelling of intertidal mudflats: the role of cross-shore tidal currents. Continental Shelf Research 22, 1887–1895.

Ralston, D.K., 2005. Hydrodynamics and scalar transport in subtidal channels through intertidal mudflats. Ph.D. Thesis, University of California, Berkeley.

Ralston, D.K., Stacey, M.T., 2005. Longitudinal dispersion and lateral circulation in the intertidal zone. Journal of Geophysical Research-Oceans 110 (C07015), 17.

Ralston, D.K., Stacey, M.T., 2007. Tidal and meteorological forcing of sediment transport in tributary mudflat channels. Continental Shelf Research 27, 1510–1527.

Ridderinkhof, H., 1998. On the sensitivity of the large scale transport and distribution of fine grained sediments in a tidal basin to the formulation of the erosion–sedimentation cycle. In: Dronkers, J., Sheffers, M. (Eds.), Physics of Estuaries and Coastal Seas. Balkema, pp. 145–153.

Ridderinkhof, H., Van der Ham, R., van der Lee, W., 2000. Temporal variations in concentration and transport of suspended sediments in a channel-flat system in the Ems–Dollard estuary. Continental Shelf Research 20, 1479–1493.

Roberts, W., Le Hir, P., Whitehouse, R.J.S., 2000. Investigation using simple mathematical models of the effect of tidal currents and waves on the profile shape of intertidal mudflats. Continental Shelf Research 20, 1079–1097.

Shi, Z., Chen, J.Y., 1996. Morphodynamics and sediment dynamics on intertidal mudflats in China (1961–1994). Continental Shelf Research 16 (15), 1909–1926.

Sleath, J.F.A., Wallbridge, S., 2002. Pickup from rippled beds in oscillatory flow. Journal of Waterway, Port, Coastal and Ocean Engineering 128 (6), 228–237.

Staats, N., de Deckere, E., Kornman, B., van der Lee, W., Termaat, R., Terwindt, J., de Winder, B., 2001. Observations on suspended particulate matter (SPM) and microalgae in the Dollard estuary, the Netherlands: importance of late winter ice cover of the intertidal flats. Estuarine, Coastal, and Shelf Science 53 (3), 297–306.

Talke, S.A., 2005. An investigation on the hydrodynamics and sediment dynamics on an intertidal mudflat on Central San Francisco Bay. Ph.D. Thesis, University of California, Berkeley.

Talke, S.A., Stacey, M.T., 2003. The influence of oceanic swell on flows over an estuarine intertidal mudflat in San Francisco Bay. Estuarine, Coastal, and Shelf Science 58, 541–554.

Waeles, B., Le Hir, P., Jacinto, R.S., 2004. Modélisation morphodynamique cross-shore d'un estran vaseux. Comptes Rendus Geoscience 336, 1025–1033.

Wright, S.A., Schoellhamer, D.H., 2004. Trends in the sediment yield of the Sacramento River, California, 1957–2001. San Francisco Estuary and Watershed Science [online serial] 2 (2) (Article 2).

Yang, S.L., Friedrichs, C., Zhong, S., Ping-Xing, D., Zhu, J., Zhao, Q.Y., 2003. Morphological response of tidal marshes, flats, and channels of the Outer Yangtze River mouth to a major storm. Estuaries 26, 1416–1425.